

Article

Potential of GPM IMERG Precipitation Estimates to Monitor Natural Disaster Triggers in Urban Areas: The Case of Rio de Janeiro, Brazil

Augusto Getirana ^{1,2,*} , Dalia Kirschbaum ¹, Felipe Mandarino ³ , Marta Ottoni ⁴ ,
Sana Khan ^{1,5} and Kristi Arsenault ^{1,2}

¹ Hydrological Sciences Laboratory, NASA Goddard Space Flight Center, Greenbelt, MD 20771, USA; dalia.b.kirschbaum@nasa.gov (D.K.); sana.khan@nasa.gov (S.K.); kristi.r.arsenault@nasa.gov (K.A.)

² Science Applications International Corporation, Greenbelt, MD 20771, USA

³ Instituto Pereira Passos, Rio de Janeiro 22221-070, Brazil; felipe.mandarino@rio.rj.gov.br

⁴ Geological Survey of Brazil, Rio de Janeiro 22290-240, Brazil; marta.ottoni@cprm.gov.br

⁵ Earth System Science Interdisciplinary Center, University of Maryland, College Park, MD 20740, USA

* Correspondence: augusto.getirana@nasa.gov

Received: 17 November 2020; Accepted: 11 December 2020; Published: 15 December 2020



Abstract: Extreme rainfall can be a catastrophic trigger for natural disaster events at urban scales. However, there remains large uncertainties as to how satellite precipitation can identify these triggers at a city scale. The objective of this study is to evaluate the potential of satellite-based rainfall estimates to monitor natural disaster triggers in urban areas. Rainfall estimates from the Global Precipitation Measurement (GPM) mission are evaluated over the city of Rio de Janeiro, Brazil, where urban floods and landslides occur periodically as a result of extreme rainfall events. Two rainfall products derived from the Integrated Multi-satellite Retrievals for GPM (IMERG), the IMERG Early and IMERG Final products, are integrated into the Noah Multi-Parameterization (Noah-MP) land surface model in order to simulate the spatial and temporal dynamics of two key hydrometeorological disaster triggers across the city over the wet seasons during 2001–2019. Here, total runoff (TR) and rootzone soil moisture (RZSM) are considered as flood and landslide triggers, respectively. Ground-based observations at 33 pluviometric stations are interpolated, and the resulting rainfall fields are used in an in-situ precipitation-based simulation, considered as the reference for evaluating the IMERG-driven simulations. The evaluation is performed during the wet seasons (November–April), when average rainfall over the city is 4.4 mm/day. Results show that IMERG products show low spatial variability at the city scale, generally overestimate rainfall rates by 12–35%, and impacts on TR and RZSM vary spatially mostly as a function of land cover and soil types. Results based on statistical and categorical metrics show that IMERG skill in detecting extreme events is moderate, with IMERG Final performing slightly better for most metrics. By analyzing two recent storms, we observe that IMERG detects mostly hourly extreme events, but underestimates rainfall rates, resulting in underestimated TR and RZSM. An evaluation of normalized time series using percentiles shows that both satellite products have significantly improved skill in detecting extreme events when compared to the evaluation using absolute values, indicating that IMERG precipitation could be potentially used as a predictor for natural disasters in urban areas.

Keywords: IMERG; extreme events; precipitation; natural disaster; urban flood; landslide; soil moisture; total runoff

1. Introduction

There is a notion that disasters are outcomes of inappropriate adjustments between people and environment [1]. An example of inappropriate adjustments is the fast-urban growth observed in the past decades, putting humans in increased natural hazard risks related to environmental degradation that are intrinsic to urban development. Many large cities in developing countries lack urban planning and management, resulting in inappropriate land use, often composed of informal and irregular settlements in high hazard risk areas (e.g., along steep hills and riverbanks) [2]. Impacts of disasters in such cities are explained by the retroactive relationships between natural hazards, urbanization and social processes [3]. Floods and landslides are two types of disasters often triggered when these areas are subjected to heavy and prolonged rainfall. Total runoff, a key hydrological variable in assessing urban flood risks, is primarily related to the rainfall intensity and land use. Over urban-based impervious land surfaces, most rainfall is converted into runoff, and without proper flood management measures, such as river restoration measures [4], floods may occur. Landslides can occur within steep terrain where unconsolidated sediments or fractured rock leads to surface instability. In areas of rapid growth, such as in the impoverished areas on the outskirts or within megacities, landslide disasters can be further exacerbated by improper building of roads, houses, poor drainage, and illegal or improper digging [5–7]. Intense and/or prolonged rainfall is the predominate triggering factor in landslide-prone areas where increased soil saturation and runoff can serve to mobilize the downstream transport of debris, rock, and soil. Disaster risk mitigation in urban areas can be addressed by reducing the hazard and/or the system vulnerability through both structural and non-structural measures [2,4]. Disaster monitoring and forecasting are examples of non-structural measures that can be used to provide stakeholders with information on how to implement or improve structural measures such as river canalization, dykes and dams, or slope retrofitting as well as other non-structural measures such as flood and landslide mapping for improved characterization of past hazards, land use regulation and early warning systems.

Recent studies have proposed near real time and even real time urban flood monitoring systems through ground-based observations of water levels [8] and meteorological variables [9], weather radar combined with ground-based sensors [10], and using crowdsourcing techniques [11]. Specialized hydrological and hydrodynamic models have also been widely used to monitor urban floods [12–18]. High-resolution remote sensing data has been adopted as another way to monitor urban flood extent and depth [19,20] and used as inputs in computational models or as reference for model evaluation [21]. The majority of these modeling studies indicate that runoff accuracy is key for precisely modeling urban floods.

Near real time or early warning landslide systems primarily rely on in situ rain gauge networks to rapidly identify the rainfall necessary to potentially trigger a landslide. In the city of Rio de Janeiro, an early warning system creates alerts when peak rainfall intensities reach a threshold in order to highlight across the city where landslides are more likely to occur (<http://alertario.rio.rj.gov.br/>). Similar systems in Italy have employed a network of automated rain gauges to highlight areas at higher hazard due to landslides at the municipal and regional scale [22]. In Norway, a combination of landslide susceptibility and rainfall thresholds is used to dynamically identify potential levels of landslide hazard across different municipalities [23]. A landslide forecasting approach based on the identification of rainfall intensity–duration thresholds is proposed for the mountainous region of Rio de Janeiro State [24]. These systems typically provide information to emergency managers, civil protection and weather forecasters to alert communities of elevated landslide risk. Nevertheless, nearly all of the current landslide early warning systems in place rely on in situ gauge or radar networks to inform landslide hazard [25,26]. Kirschbaum and Stanley [27] provide a global framework for characterizing rainfall-triggered landslide hazards using satellite rainfall. However, the topic of how satellite precipitation estimates may be used to resolve extreme rainfall relevant for triggering hydrometeorological hazards at an urban scale is an area of open research.

Over twenty years of satellite-based global rainfall estimates through the Tropical Rainfall Measuring Mission (TRMM) [28] and the Global Precipitation Measurement (GPM) [29,30] mission have improved our knowledge on the global water cycle and its impacts on society [31]. Several studies have focused on the evaluation of different satellite products [32–35] and their usefulness as a model input to simulate the water and energy balance [36–38]. Although satellite-based rainfall estimates have been widely evaluated at large scales [39–41], few studies have focused at local scale hydrometeorological extremes. An evaluation of TRMM Multi-satellite Precipitation Analysis (TMPA) [28] and Integrated Multi-satellite Retrievals for GPM (IMERG) [42] rainfall estimates over Singapore, using observations at 48 pluviometric stations as reference, concluded that daily satellite products show moderate correlation with gauge data and underestimate heavy rainfall events [43]. Another evaluation of one storm event over Attica, Greece, showed that IMERG underestimated both rainfall and its subsequent flood event [18]. These studies suggest that such products are generally not adapted to monitor local scale rainfall heterogeneities at shorter timescales (i.e., sub-daily and daily), which are essential for urban disaster monitoring. However, such a suggestion is inconclusive, due to the restricted number of studies and limited coverage. Furthermore, there remains an open question in the field as to how satellite precipitation estimates may be leveraged to identify and characterize high-impact hydrometeorological events at a city scale.

The focus for this study involves the municipality of Rio de Janeiro (RJ), Brazil, and has been developed as part of a pioneering partnership between NASA and the city to advance natural disaster monitoring capabilities at the city scale. As part of this partnership, RJ has been providing critical in situ data used in combination with NASA datasets and tools to further parameterize and test modeling frameworks designed to monitor and forecast floods and landslides. Spanning 1204 km² in area, RJ is located in Southeastern Brazil (Figure 1a) and stands as the second largest city in the country and ranked fifth in Latin America. The city has witnessed a significant urbanization rate in the past few decades, where 6.72 million people live. Part of this urban expansion is composed of informal settlements, mostly in steep hills within the city. More recently, informal settlements have also been spreading in flat flood-prone areas. RJ has historically suffered from massive rainstorms and subsequent floods and landslides, all of which have caused casualties and adverse socioeconomic impacts. For example, heavy storms with rain accumulations of 90 mm within one hour and wind gusts of around 110 km/h impacted the city between 6–7 February and 7–8 April 2019, causing floods and landslides, and killing numerous people [44–47].

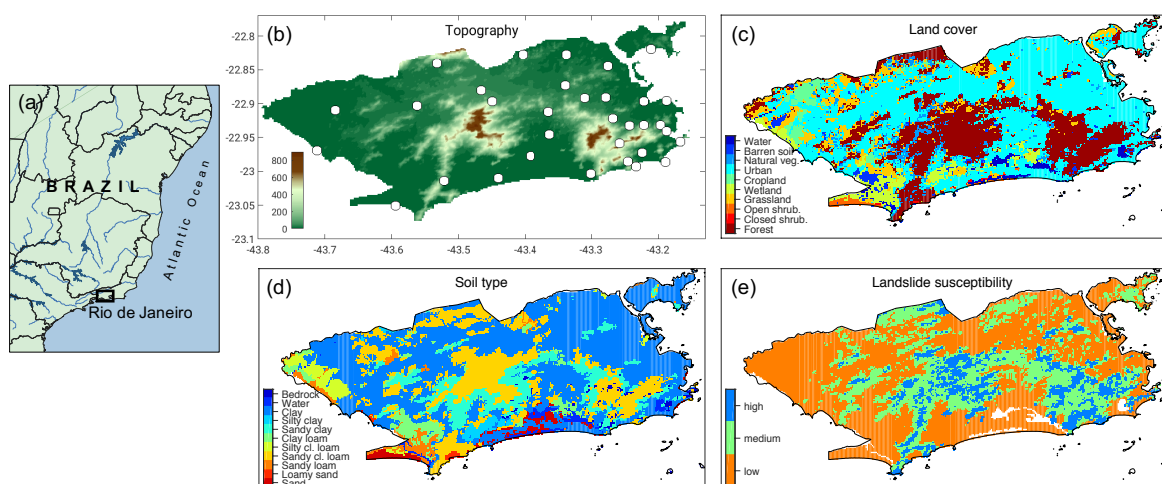


Figure 1. Study area/geographic location, and land surface datasets available for Rio de Janeiro city: (b) topography, (c) land cover, (d) soil type and (e) landslide susceptibility maps. The spatial distribution of pluviometric stations is also provided in panel (a).

This study is motivated by this NASA-RJ partnership's efforts to develop a near real-time disaster monitoring system for Rio de Janeiro, and our current limited understanding on satellite capabilities to monitor local scale rainfall heterogeneities. Here, we aim to test the concept of how IMERG precipitation estimates can inform hydrometeorological modeling capabilities for natural disasters at a city scale, and their impact on simulating processes that influence floods and landslides within urban areas. We define urban rainfall-related disasters as floods and landslides, and their hydrometeorological related triggers as total runoff (TR) and rootzone soil moisture (RZSM). Here, RZSM is defined as the soil layer one meter below the land surface. A state-of-the-art land surface model (LSM) is used to simulate hydrological processes over the city, and rainfall fields, derived from the interpolation of ground-based observations, are used as the reference for the evaluation. We first investigate how well IMERG products and gauges match across the city, and whether they are capable of detecting major events that occurred in the region during the wet seasons from 2001 to 2019. Wet seasons are defined as the period between November and April, when most storms take place. Then, we evaluate the potential of IMERG products as a predictor of TR and RZSM variables, derived from modeling experiments using LSM outputs. This evaluation is performed across the city and over urban and landslide-prone areas. Finally, we evaluate IMERG precipitation during two recent extreme events, which occurred in February and April 2019. Details on the datasets and methods adopted in this study, results, and conclusions are provided in the following sections.

2. Datasets and Methods

2.1. Modeling Framework

The modeling framework designed for RJ used the NASA Land Information System (LIS) [48] where multiple LSMs are implemented. LIS allows the integration and assimilation of multiple satellite datasets into LSMs, including IMERG rainfall estimates. Land model parameters were processed using the Land surface Data Toolkit (LDT) [49]. The LSM, as well as datasets used in this study, experimental design and evaluation procedure are described next.

Noah-MP

The Noah Multi-Parameterization (Noah-MP) [50,51] land surface model, version 4.0.1, is used to simulate the vertical water and energy balances over the city. The Noah-MP LSM builds upon the well-known Noah LSM [52], which has been used in a variety of operational models, applications and research studies. Noah-MP contains four soil layers and different parameterization and physics options, which include different static vegetation and dynamic vegetation schemes, canopy resistance effects, radiation transfer (e.g., two-stream approximation), runoff and groundwater schemes, snow model options, and even crop and urban canopy schemes. We apply the dynamic vegetation scheme, which employs the Ball-Berry canopy and stomatal-resistance option [53] and Noah-based soil moisture factor for stomatal resistance. The TOPMODEL simulated groundwater scheme [54] is selected, and the Noah-based lower boundary of soil temperature option is applied. For the crop and urban physics schemes, these were not applied at this time, since their physics require more review prior to application in LIS. However, to represent more realistic impervious surface responses, land use and soil types related to urban grid-cells were treated as "bedrock", based on suggested parameters in [55] and assigning a slightly higher porosity for these points. According to Schueler [56], the porosity of urban soils varies between 17% to almost 40%. In this sense, an average porosity of 28% to represent urban areas is a valid assumption. The soil configuration simply used the dominant soil texture type map. Other climatology-based vegetation and albedo parameter maps include monthly greenness fraction [57] and global (snow-free) albedo [57]. Table 1 summarizes the main schemes used in Noah-MP.

Table 1. Noah-MP options adopted in this study to represent physical processes.

Physical Process	Noah-MP 4.0.1 Options	References
Vegetation	Dynamic simulation of carbon uptake and calculated by partitioning LAI and shade fraction (Option 2)	[51]
Stomatal resistance	Ball-Berry (Option 1)	[53]
Soil moisture factor for stomatal resistance	Noah-type based on soil moisture (Option 1)	[58]
Runoff & groundwater	SIMGM: based on TOPMODEL (Option 1)	[54]
Surface layer drag coefficient	Monin-Obukhov (Option 1)	[59]
Super-cooled liquid water	Standard freezing point depression (Option 1)	[60]
Radiation transfer	Modified two-stream scheme (Option 1)	[61]

Note: Cold-season related processes and options (e.g., snow fall, accumulation and depth) are not included here.

2.2. Meteorological Datasets

Noah-MP was forced with the operational Global Data Assimilation System (GDAS) meteorological analysis dataset, IMERG and rainfall fields derived from pluviometric stations. These datasets are described below.

IMERG

IMERG is an algorithm that fuses information from multiple sources, including satellite microwave and infrared precipitation estimates and ground gauge information. The IMERG algorithm uses several passive microwave sensors to assemble and intercalibrate precipitation estimates. However, due to the limited sampling of passive microwave sensors on low-earth-orbit platforms, the gaps are filled by microwave-adjusted infrared estimates [62]. The IMERG algorithm is run three different times, generating the following multi-satellite products: (i) IMERG Early (IMERG-E), available ~4 h after the satellite observation time, allowing quick assessment for flood and landslide prediction; (ii) Late, available ~12 h after the observation time, mainly for agricultural applications; and (iii) Final (IMERG-F), available ~2 months after observation, once monthly gauge data become available, for research applications. IMERG Early and Late are calibrated with climatological sets of coefficients that vary by month and location, and IMERG Final is adjusted with monthly gauge observations. Global data fields are available for 2001-present and provided by the NASA Precipitation Processing System at 0.1° spatial resolution and at a 30-min time step. About 20 IMERG pixels covering the city were spatially interpolated to 0.002 degrees (approximately 200 m) using the budget-bilinear approach.

Pluviometric Stations

Rainfall has been measured operationally every 15 min since 1997 at 33 pluviometric stations within the city. Their spatial distribution is heterogeneous, mainly concentrated in the more developed eastern portion of the city where there is a higher concentration of informal settlements on hills, hence more prone to landslides. Fewer stations are located in the less developed western side (locations are shown in Figure 1b), where informal settlements occupy flat and often flood-prone areas. The inverse distance squared weighting approach [63] was used to spatially distribute point-based rainfall observations throughout the city at a 0.002-degree spatial resolution and 30-min time step. Morphology was taken into account following a similar approach suggested by Salvatici et al. [64], where the domain is divided into sub-regions composed of catchments limited by geomorphological features and the interpolation is performed using only rainfall observations within sub-regions. Here, the city was *divided* into four catchment-based sub-regions, which are representative of the city's morphology: West, South, Southeast and Northeast.

2.3. Land Surface Parameterization

Key land surface parameters used in Noah-MP, in particular, topography, land cover and soil type, were acquired from local measurements and high-resolution airborne and satellite imagery, and they are described below and shown in Figure 1. A landslide susceptibility map, used in the analysis of results, is also described.

Topography

Lidar data used for the model was acquired through an aerial survey in the second half of 2019, with a raw density of eight points per square meter. Point-based cloud data was filtered for ground-only returns and interpolated as a 15-cm spatial resolution digital terrain model map. For the purpose of this study, the hyper-resolution data were resampled to 0.002 degrees.

Land Cover

Local land cover data were acquired from the City's Government Environment Secretariat, reference year 2016, as a vectorial database at a 1:10,000 cartographic scale. The vectorial database was reclassified following the International Geosphere–Biosphere Programme (IGBP) [65] land cover classification and converted to a 0.002-degree raster map. According to the resulting map, urban areas represent 50% of the city's land use.

Soil Type

The Rio de Janeiro soil map was derived from 41 soil mapping units at the scale of 1:50,000, updated by Gomes et al. [66]. According to this study, Ultisol (also called Alfisol) soil class predominates in the domain, followed by Oxisols [67] in, respectively, 40% and 17% of the region. A representative soil textural class, according to the American textural classification system [68], was assigned to each of the mapping units, taking into account granulometric fractions information (sand, silt and clay content) of representative soil profiles obtained according to Embrapa [69]. The sandy loam class from indiscriminate mangrove soils was assigned based on the literature on these soils. This study allowed the estimation of the different hydraulic parameters for RJ soils required by the model, taking its standard tables that associate textural classes with the referred hydraulic parameters as reference.

Landslide Susceptibility Map

Rio de Janeiro's landslide susceptibility map is available at a 5-meter spatial resolution as a result of a multicriteria spatial analysis based on the overlapping of the following layers: lithology, soil type, slope, land cover, geotechnics and geomorphology. The susceptibility map was developed by GEORIO, the municipal geological service, and is based on site investigations and expert analysis [70]. Three classes are defined in the map: low, medium and high susceptibilities. Here, we adopted classes medium and high as landslide-prone areas, corresponding to 42% of the city's surface area.

2.4. Experimental Design

To determine the potential of IMERG products to monitor TR and RZSM throughout the city, three experiments were designed: one using ground-based precipitation (called the reference experiment hereafter), and two using IMERG datasets, called IMERG-E and IMERG-F experiments hereafter. Since our goal is to explore the potential for IMERG to monitor natural disasters at the near real-time and possibly to be used to generate initial hydrological conditions for forecasts, IMERG-F is considered here as a benchmark for IMERG-E, due to its relatively long latency and inclusion of ground-based observations. In order to isolate the impact of IMERG products on the hydrological modeling, all experiments were composed of the same land surface parameters and GDAS meteorological forcings, except for the rainfall data. Experiments were run for 19 years, from 2001 to 2019, where all meteorological datasets overlap, on a 30-min time step and 0.002-degree spatial resolution. GDAS data was time-interpolated using linear weights to bring it down to the 30-min time step. Land surface parameters described above were also rescaled to 0.002 degrees, matching the spatial resolution of the modeling system. The spatial and temporal resolutions adopted here are sufficiently fine to represent fine-scale physical processes of interest. Experiments were spun up for 50 years, allowing modeled water storage states to stabilize.

2.5. Evaluation Procedure

The lack of in situ data and insufficiently high-resolution satellite-based soil moisture and runoff observations prevents us from evaluating model outputs against an observable truth. In the absence of such observations, we compared IMERG experiments against the reference experiment, as it could be considered as the most accurate representation of precipitation over the domain. Floods and landslides are mostly triggered by extreme rainfall events, mostly common during the wet season. Here, we defined the months from November to April as the wet season and focused all analyses on that period, neglecting events that may have occurred in other months. The IMERG evaluation was performed daily at both point-based and city-wide scales, using metrics such as bias, root mean square error (RMSE), and correlation. The evaluation of extreme event detection skill was performed by using two categorical metrics: the probability of detection (POD) and false alarm rate (FAR). POD defines the rate of correct satellite-based rainfall estimates, while FAR is the rate of false ones, as defined below:

$$\text{POD} = \frac{a}{a + c} \quad (1)$$

$$\text{FAR} = \frac{b}{b + d} \quad (2)$$

where a is the number of simulated events above the threshold correctly observed, b stands for the number of false alarms (simulated events above the threshold detected but not observed), c is the number of simulated events above the threshold not observed, and d is the sum of events above the threshold neither observed nor simulated. POD values range from zero to 1, where zero corresponds to no skill in correctly detecting events and 1 stands for a skillful system correctly detecting all events. FAR values also range from zero to one, where zero is the ideal case, meaning that no events were wrongly detected, and 1 indicates that events were wrongly detected throughout the study period.

For the point-based evaluation, we categorized the extreme events into three classes according to different rainfall thresholds [71,72]: moderate rain (≥ 10 mm/day), heavy rain (≥ 25 mm/day) and torrential rain (≥ 50 mm/day). Next, we evaluated the accuracy of spatially-distributed precipitation estimates and their impact on simulated rootzone soil moisture and total runoff by means of correlation, root mean square error (RMSE), POD and FAR. For the spatial analysis, thresholds were defined as percentiles rather than absolute values. Percentile thresholds are commonly used for extreme event monitoring and forecast [73–76]. Percentiles were computed for each pixel from each experiment, individually, using the full 2001–2019 period (i.e., dry seasons were also considered). By considering the full period, which includes a large quantity of low or no rain events during the dry seasons, it can impact percentiles in a way that extreme events become rarer, thus higher percentile values. Daily rainfall, RZSM and TR over the full period (i.e., a total of 6939 daily events per grid cell) were ranked and converted to their corresponding percentiles, from 1% (least severe wet events) to 100% (most severe wet events). Finally, five percentile thresholds of varying likelihood of occurrence were defined: abnormally wet ($\geq 70\%$), moderately wet ($\geq 80\%$), severely wet ($\geq 90\%$), extremely wet ($\geq 95\%$), and exceptionally wet ($\geq 98\%$).

3. Results

3.1. Point-Based IMERG Evaluation

Point-based comparisons at 33 pluviometric stations indicate that both IMERG products overestimate rainfall estimates during wet seasons throughout the city, with median biases of 0.66 mm/day for IMERG-E (Figure 2a) and 1.6 mm/day for IMERG-F (Figure 2d). The higher bias obtained with IMERG-F could be explained by corrections using ground-based observations. Brazil's nationwide rain gauge network [77], normally available for the international scientific community, is not available in Rio de Janeiro and remains scarce in the surrounding region. This network also excludes the municipal rain gauge network used in this study. Such a geographic limitation may result in biases over

coastal areas where orographic and other meteorological processes dominate precipitation patterns and where the satellite retrieval algorithms may be less sensitive to land-ocean background states. Biases with respect to rain gauges could result from the positioning of the gauges lower down on the slopes where peak intensities may not be resolved, or from gauge under catch resulting from wind or debris on the gauge. One station stands out with a high negative bias (i.e., satellite estimates are lower than observations) of -2.66 mm/day and -1.78 mm/day, respectively, in Southeast RJ. That station is situated at 355-m high on steep hills near the coast where landslides are frequent, and neighbourhoods downstream often flood during storms. RMSE values are high relative to the average rainfall, varying from 10.4 to 19.5 mm/day, depending on the station and satellite product (Figure 2b,e). Daily IMERG products show moderate correlation with gauge data, varying from 0.38 and 0.58 (Figure 2c,f) and median correlation values of 0.49 (IMERG-E) and 0.54 (IMERG-F). These results are consistent with the point-based skill evaluation, revealing a moderate POD for events greater than or equal to 10 mm/day, averaging 0.53 and 0.6, respectively (Figure 3a,d). Overall, IMERG-F indicates more skill in detecting extreme events than IMERG-E, although it has higher bias and RMSE values. POD values degrade for higher rainfall thresholds greater than or equal to 25 and 50 mm/day, averaging 0.33 and 0.16 for IMERG-E and 0.44 and 0.24 for IMERG-F. As shown in Figure 3g–l, false alarm rates of extreme events are high for both satellite products and all selected thresholds, with FAR averages varying from 0.57 (rainfall ≥ 10 mm/day) to 0.8 (rainfall ≥ 50 mm/day). High FAR values indicate that high rainfall rates are detected by IMERG, but not observed, which could explain the positive bias and high RMSE discussed above.

3.2. IMERG Impacts on Total Runoff and Rootzone Soil Moisture Simulations

Figure 4 shows the spatially-distributed averages of rainfall, RZSM and TR over the city during wet seasons derived from the spatial distribution of reference pluviometric data and IMERG products, and corresponding monthly climatologies. Based on the reference rainfall, the average precipitation over RJ is 4.43 mm/day, with a heterogeneous spatial distribution, varying from 3.65 to 7.47 mm/day. The spatial variability of RZSM derived from the reference rainfall reflects the land cover classification and soil composition, with low average values over urban areas (0.13 m³/m³), explained by the low infiltration rates as a result of the impervious urban land cover, and high over landslide-prone areas (0.26 m³/m³). RZSM averages 0.21 m³/m³ over the city. Generally, high soil moisture variability means more infiltration during rain events, resulting in more water available for evapotranspiration, hence less available surface water to run off. This is evident in the model simulation, where average TR is 4.33 mm/day (or 97% of rainfall) over urban areas, and 0.65 mm/day (15% of rainfall) over landslide-prone areas.

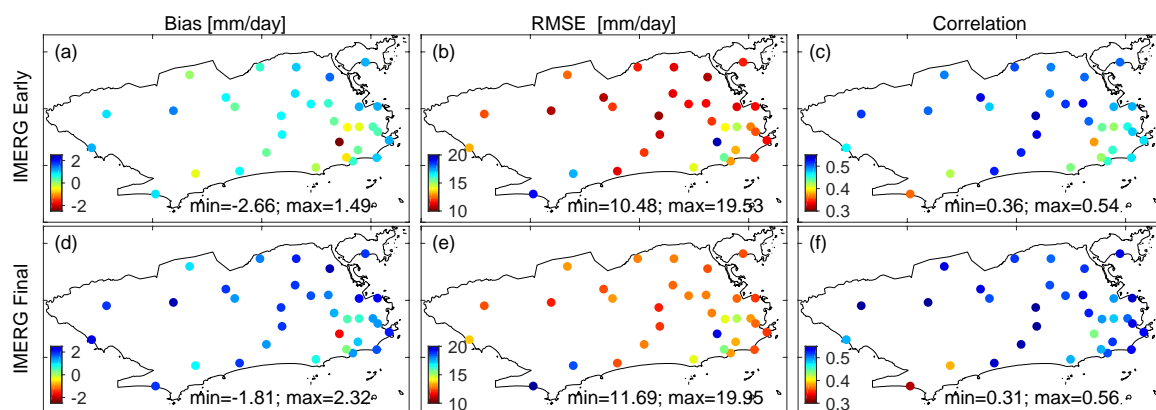


Figure 2. Daily bias, root mean square error (RMSE) and correlation for IMERG Early (a–c) and IMERG Final (d–f) at 33 pluviometric stations for 2001–2019 wet seasons (November–April). Limits of Rio de Janeiro city are defined by the black line.

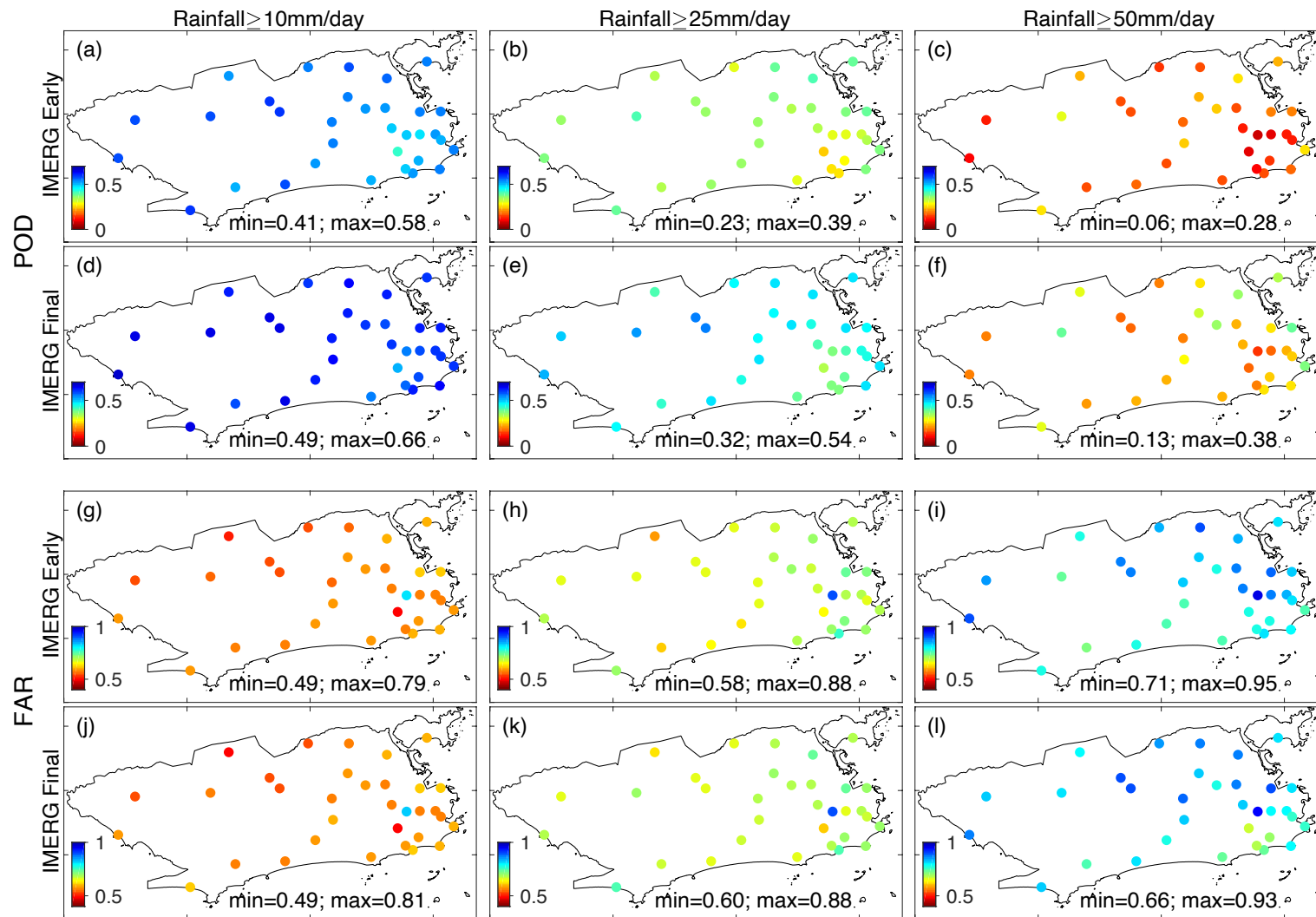


Figure 3. Probability of detection (POD) and false alarm rate (FAR) maps at three rainfall thresholds (≥ 10 mm/day, ≥ 25 mm/day and ≥ 50 mm/day) for IMERG Early (a–c,g–i) and IMERG Final (d–f, j–l) at 33 pluviometric stations for 2001–2019 wet seasons.

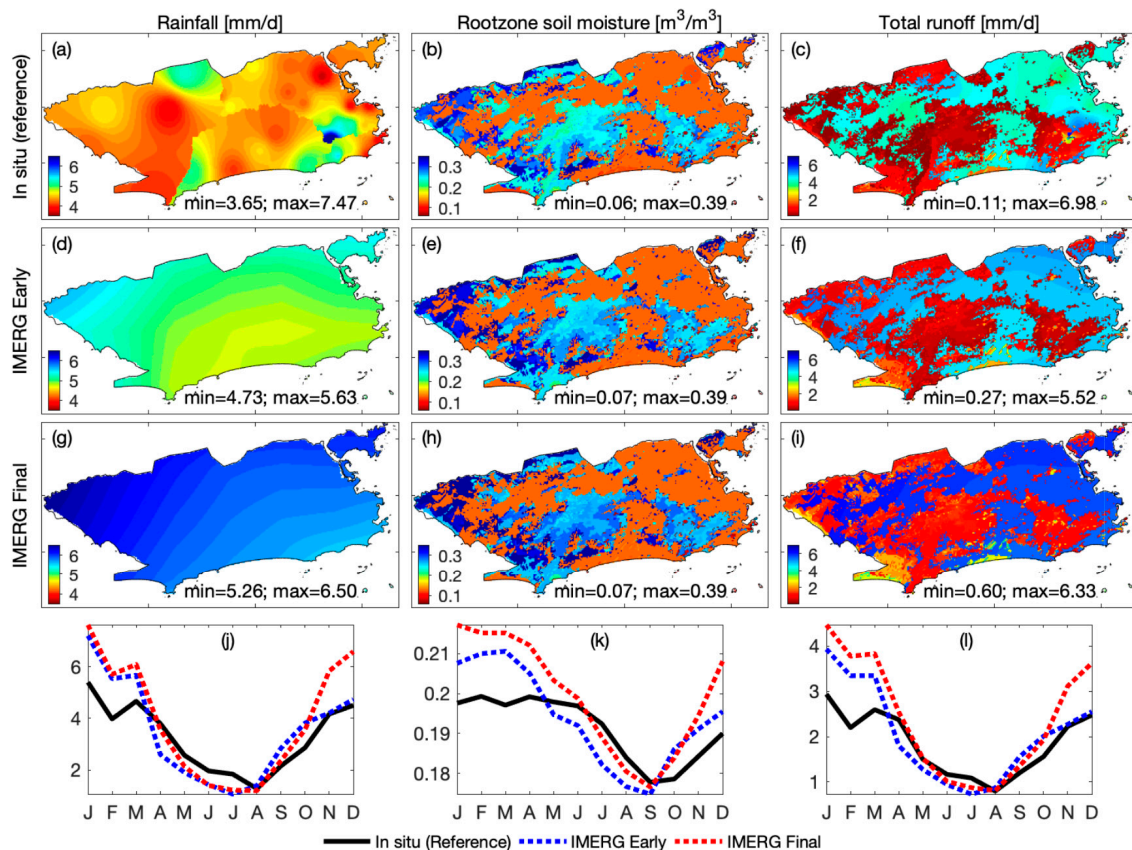


Figure 4. Spatially distributed rainfall, rootzone soil moisture (RZSM) and total runoff (TR) averaged over 2001–2019 wet seasons derived from the experiments using ground-based (a–c), IMERG Early (d–f) and IMERG Final (g–i) rainfall estimates. Spatially-averaged monthly climatology time series are shown in the bottom (j–l).

Although IMERG products overestimate average rainfall over the city during wet seasons by about 12% or 5.01 mm/day (IMERG-E), and 35% or 5.93 mm/day (IMERG-F), they both show low spatial variability. This could be a result of IMERG’s insufficiently fine spatial resolution to represent local heterogeneities. Monthly climatologies show that IMERG overestimates rainfall during most of the wet season, except April. Such differences in rainfall have little impact on average RZSM, but significantly impacts TR, especially over urban areas, with average increases ranging from 14% to 34%. As a result, RMSE for the spatially distributed rainfall is high, varying from 9 to 19.4 mm/day (Figure 5a,d), similarly to those found for the point-based evaluation. RMSE is particularly high in the city’s coastal south-eastern hilly extents, a rainfall hotspot where observations are much higher than the city average. IMERG products also show the lowest correlation with the reference rainfall over that location, varying between 0.38–0.45. Except for the rainfall hotspot, correlation over most of the city ranges from 0.5 to 0.64, with IMERG-F performing generally better than IMERG-E. Despite the moderate IMERG performance in providing spatially distributed rainfall estimates over the city, RZSM is not as degraded, with relatively low RMSE values, ranging from zero to 0.09 m³/m³, and higher correlation, varying from 0.41 and 0.86, depending on the satellite product and location. On the other hand, TR is highly degraded, in particular in the south-eastern extent of the city, with RMSE values as high as 16.7 mm/day and correlation as low as 0.23.

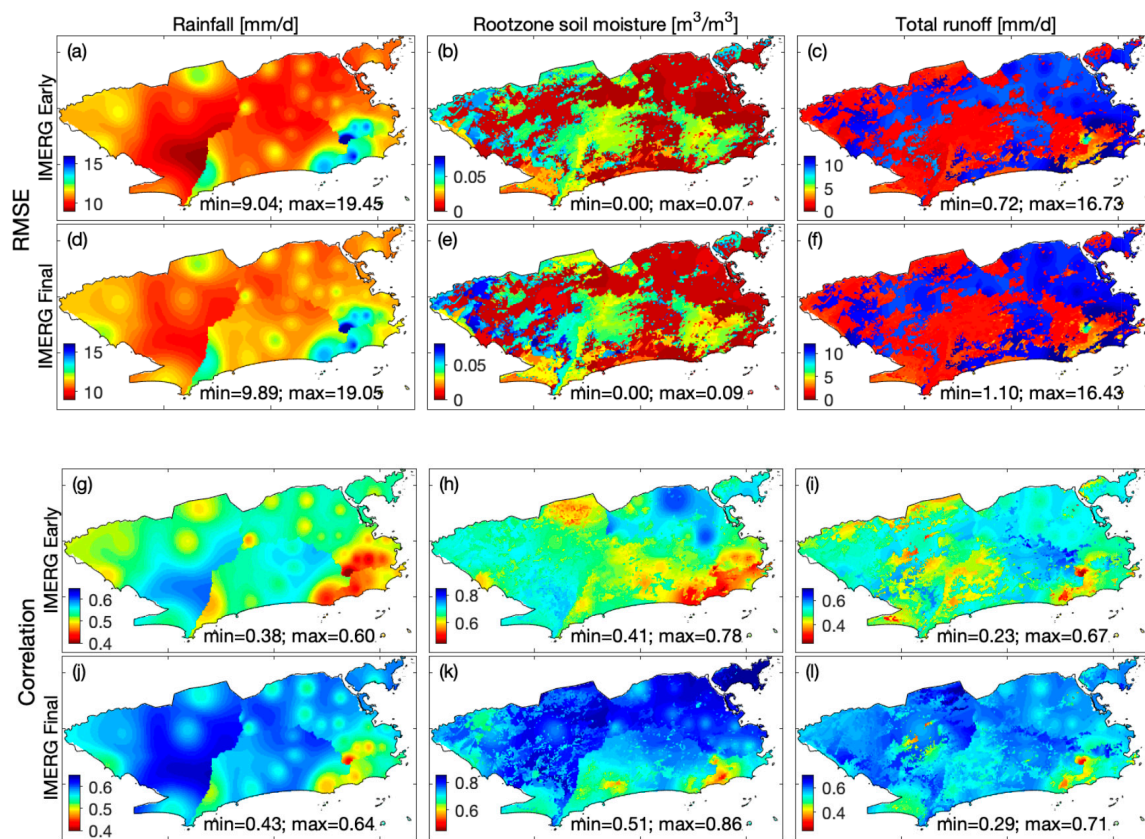


Figure 5. Spatially distributed RMSE and correlation of absolute rainfall, rootzone soil moisture and total runoff estimates over 2001–2019 wet seasons. Results are shown for experiments with IMERG Early (a–c,g–i) and IMERG Final (d–f,j–l).

Figure 6 summarizes the results for the full domain, landslide-prone and urban areas. A comparison of performances between satellite products reveals that IMERG-E has lower RMSE values over the three regions but low correlation, indicating that it has better skill in estimating rainfall magnitudes and not in rainfall timing. RMSE is basically the same for both IMERG-based RZSM estimates and very similar for TR estimates, while IMERG-F shows an overall better performance in terms of correlation. Over landslide-prone areas, where RZSM is a disaster trigger, RMSE is low relative to the average soil moisture and correlation is higher than those obtained for rainfall estimates. On the other hand, TR over urban areas does not perform as well. Although the western extent of the city is poorly monitored, it shows an overall better performance in term of RMSE and correlation, possibly due to the lower irregular geomorphology.

3.3. Evaluation of Selected Events

We selected two major storms to further evaluate the potential of IMERG in detecting natural disaster triggers in urban areas. They occurred on 5–7 February 2019 (Event 1) and 9–10 April 2019 (Event 2) and resulted in floods and landslides, causing major socio-economic damage in the city. Figure 7 shows hourly rainfall from the reference and IMERG products and their impact on TR over urban and RZSM over landslide-prone areas for both events. In Event 1, two rainfall peaks are observed two days apart, reaching 15 mm/h. Although the first one was detected by IMERG, both satellite products underestimate the total rainfall by about half. The second peak is missed by IMERG, showing smaller rainfall events distributed over 24 h instead. Over urban areas, the total observed rainfall during Event 1 was 128 mm, as opposed to a much lower amount of 71 and 62 mm detected by IMERG-E and IMERG-F, respectively. Such low IMERG-based rainfall rates resulted in 45–51% TR underestimation. Over landslide-prone areas, the reference experiment shows two consecutive RZSM

raises within 2 days, occurring during each rainfall peak and totalling a soil moisture increase of 65%. The soil saturation caused by the second raise occurred in 6–7 February concomitant with the surging of numerous landslides over the city [45]. High RZSM levels derived from IMERG-based experiments at the beginning of Event 1 are explained by an early storm detected by IMERG, peaking ~10 mm/h, but not observed (not shown). As a result, the low rainfall peak was enough for RZSM to reach the reference level at the end of the first peak, but not to rise to the maximum reference moisture at the end of the second peak. Event 2 was characterized by a 2-day-long storm, totalling 201 mm of rainfall across the city (193 mm over urban areas and 213 mm over landslide-prone areas), with 183 mm during the first 24 h. This storm had three peaks with decreasing magnitudes over time. Both satellite products successfully detected the two major ones, but IMERG-F performed better, with a total rainfall of 122 mm, as opposed to 69mm with IMERG-E. The underestimated rainfall resulted in 36–64% lower TR over urban areas. Although slightly underestimated, soil moisture signals were properly represented, in particular by IMERG-F rainfall. The results obtained for these two cases suggest that, although IMERG products overestimate the average rainfall across the city, some severe storms might still be underestimated.

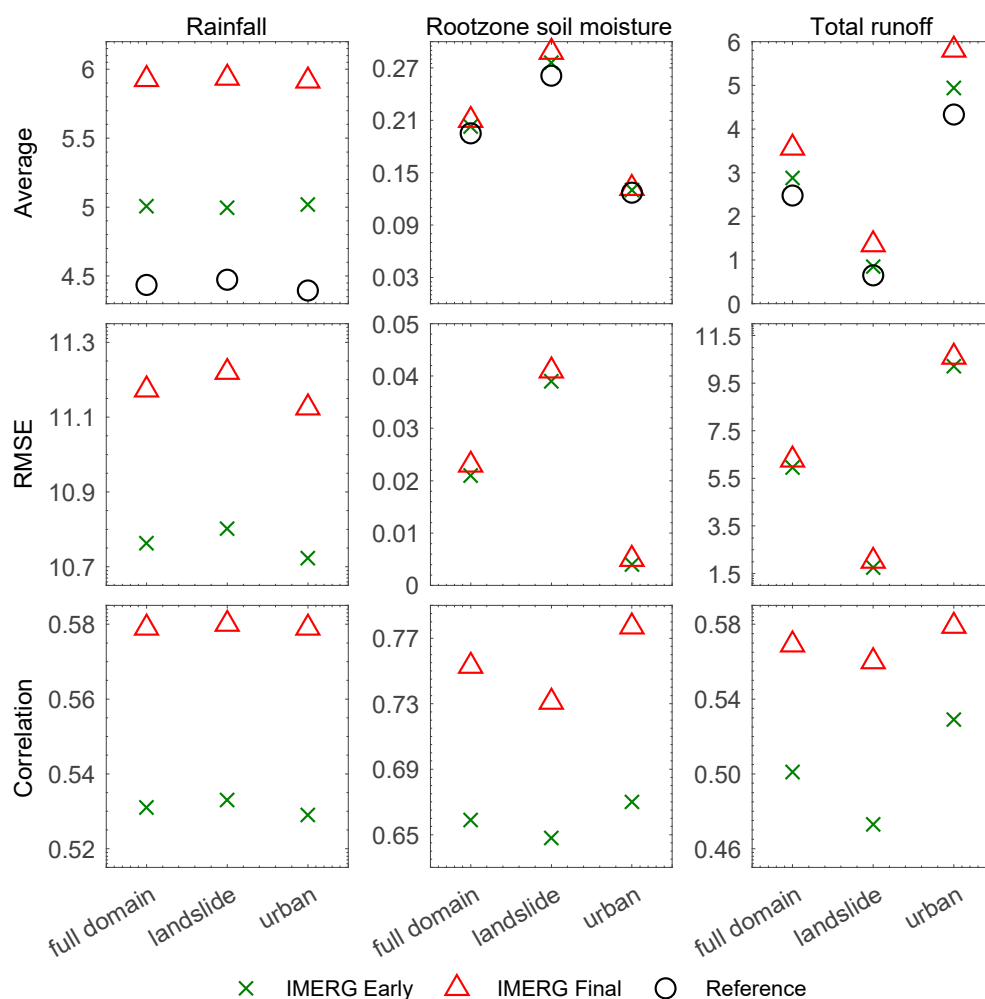


Figure 6. Average, RMSE and correlation of precipitation, rootzone soil moisture and total runoff derived from experiments using ground-based, IMERG Early and IMERG Final precipitation estimates. Results are shown as medians for 2001–2019 wet seasons over the full domain, and landslide-prone and urban areas. Average and RMSE units are mm/day for rainfall and total runoff, and m^3/m^3 for rootzone soil moisture.

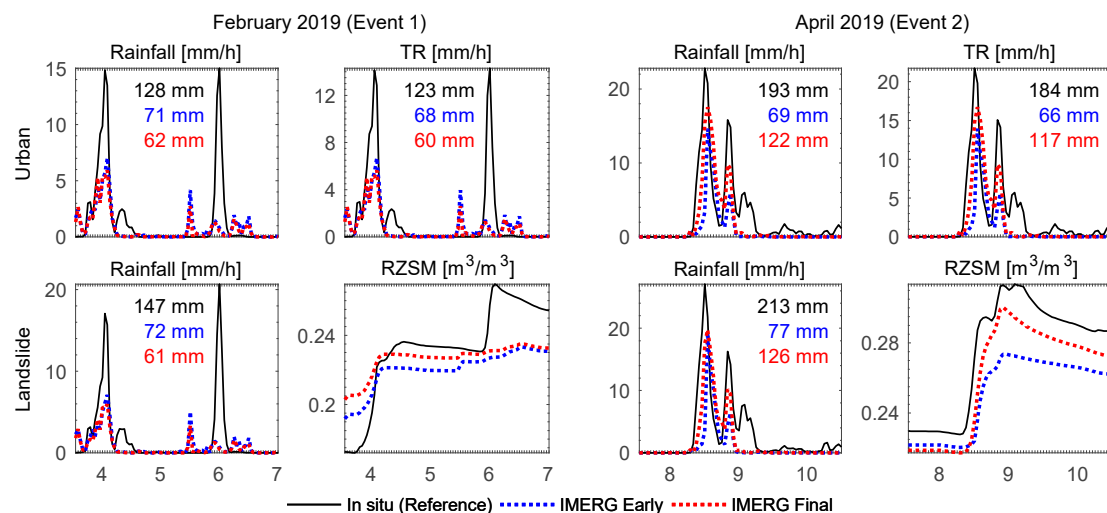


Figure 7. Selected storm events in Rio de Janeiro city and impacts on total runoff (TR) and rootzone soil moisture (RZSM) over urban (top) and landslide-prone (bottom) areas. Left panels show the evolution of the storm occurred from 5–7 February 2019 (Event 1), and right panels show the storm that occurred in 9–10 April 2019 (Event 2). Results are shown at the hourly time step and x-axes indicate days of the month.

3.4. Detection Skill of Extreme Events in Terms of Percentiles

Based on the evidence of an overall mismatch between reference-based and IMERG-based extreme events in terms of the total mm/day, we considered event detection evaluation in terms of percentiles. Using percentiles is a way to normalize time series independently, based on the magnitude of the events, and remove any biases found between two independent sources. In this way, it helps us understand IMERG's skill to detect daily extreme categorical events, even if the magnitudes differ. As an example, Figure 8 shows the spatial distribution of POD and FAR for normalized rainfall, RZSM and TR at a percentile threshold $\geq 70\%$, i.e., panels show the probability of IMERG-based hydrometeorological variables to detect or provide a false alarm of an event that is 70% or higher than all events in the time series at each pixel (POD and FAR maps for percentile thresholds $\geq 80\%$, $\geq 90\%$, $\geq 95\%$ and $\geq 98\%$ are shown in Figures S1–S4). Based on similar maps for all five thresholds, as defined in Section 2.5, we computed medians of percentile-based POD and FAR values over urban and landslide-prone areas for each IMERG-based experiment. As summarized in Figure 9, we can observe that percentile-based POD and FAR are significantly higher than those obtained using absolute values of rainfall, TR and RZSM. This demonstrates that, although IMERG-based experiments moderately detect event magnitudes, it shows higher skill in detecting occurrences. However, both POD and FAR degrade as a function of rainfall intensity. Median POD values range from 0.75 to 0.84 for abnormal ($\geq 70\%$) hydrometeorological events (i.e., rainfall, TR and RZSM) occurring over urban and landslide-prone areas and degrade to 0.28–0.42 for exceptional events ($\geq 98\%$). This means that the more exceptional the event is, less likely IMERG will detect it. IMERG-F skill to detect extreme events is slightly higher. Median FAR values are generally low, ranging from 0.2 to 0.29 for abnormal events, improving to 0.02 for exceptional events. Such an improvement is explained by the fact that the more exceptional the event is, larger the ensemble of non-observed events will be. All thresholds below 95% show that IMERG experiments provide fewer false alarms for rainfall than RZSM over landslide-prone areas, indicating that IMERG generally overestimates low rain events during the wet seasons, resulting in more RZSM extreme events than observed. Rainfall and TR show similar FAR for all thresholds, confirming the high correlation between these two variables over urban areas.

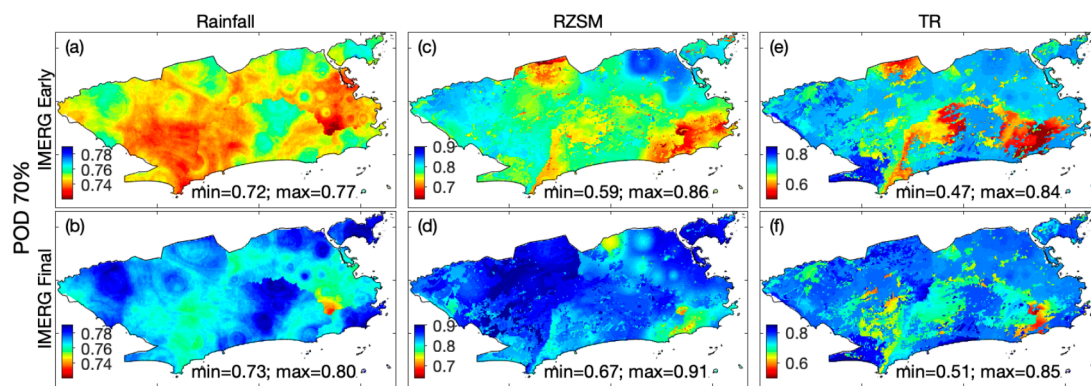


Figure 8. Probability of detection (POD) and false alarm rate (FAR) maps for rainfall (a,b), rootzone soil moisture (RZSM) (c,d) and total runoff (TR) (e,f) events derived from experiments with IMERG Early and IMERG Final at the percentile threshold 70% chance of occurrence.

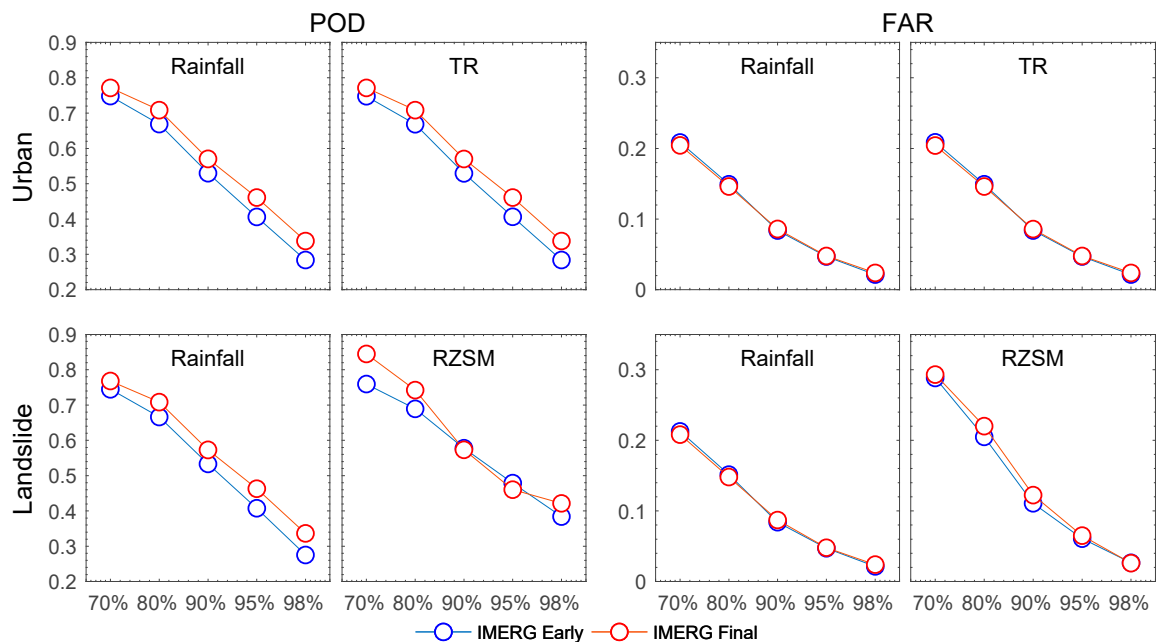


Figure 9. Median POD and FAR for rainfall, rootzone soil moisture (RZSM) and total runoff (TR) rates derived from IMERG-E and IMERG-F experiments at percentile thresholds of $\geq 70\%$, $\geq 80\%$, $\geq 90\%$, $\geq 95\%$ and $\geq 98\%$ over the urban and landslide-prone areas.

4. Discussion

It is important to highlight that although we used ground-based rainfall observations as the reference for this analysis, the gauging network spatial distribution does not represent all climatologic and geographic heterogeneities found in the city. The complex topography within RJ creates microclimates that cause rainfall accumulations to significantly vary across the city. Rainfall totals can differ based on the prevailing wind patterns of the storms and where the storms originate and move, further complicating the ability to systematically define local maxima in rainfall. The orographic enhancement of these systems resulting from the complex topography and microclimates within the city further complicate the ability to get a complete and accurate representation of total rainfall across the city. The geographic distribution of the 33 pluviometric zones are primarily located in low elevations, which could result in an underestimation of the actual precipitation over the city. There is also a sparser gauge network in the western portion of the municipality, which may impact the total accumulations of gauge-based estimates when comparing averages across the city. However, there are

also known challenges in comparing satellite estimates with individual observations from rainfall gauges for a number of reasons. First, the IMERG data is composed of integrating passive microwave estimates from a constellation of approximately 10 satellites that are in non-synchronous or polar orbits. These observations are then merged, morphed and filled in with infrared data from geostationary satellites. If there is a short convective storm that has high rainfall intensities, but which develops and dissipates within 30 min, unless there is a passive microwave sensor observing that storm directly, there is a chance that the satellite product could partly or entirely miss the event. This likely is why we observe IMERG resolving a portion of the extreme rainfall but not resolving the entire event, hence underestimating the total storm volumes.

The sparse number of gauges in the western part of the city and the interpolation technique used to generate the reference rainfall fields are other factors impacting the accuracy of the reference rainfall fields. Here, we assumed that the inverse distance squared weighting approach constrained by catchment-based sub-regions was sufficient to take morphology into account and accurately spatialize point-based rainfall observations. However, we acknowledge that this technique has restrictions by not considering all topographic and coastal effects. Such restrictions, in addition to limitations in the land parameterization and numerical representation of physical processes in Noah-MP, may result in inaccurate estimates of water storages and fluxes. For example, due to the unavailability of an urban hydrology module in the Noah-MP available in LIS, we used the “bedrock” soil class to represent urban imperviousness. Although this could emulate the impacts of urbanization on water fluxes and storage, it is not ideal to represent impacts buildings on the energy balance [78]. It also is important to note that, since Noah-MP does not store TR from a time step to another, surface water is not available for further evaporation after rain events. Hence, the actual TR could be lower during prolonged floods.

5. Summary and Final Considerations

Previous studies have successfully demonstrated that satellite precipitation can be used at large and mesoscale hydrometeorological monitoring and modeling with sufficient accuracy [79–81]. Motivated by the current limited understanding of how satellite-based rainfall estimates perform at local scales, in particular over urban areas, and taking advantage of a partnership between NASA and Rio de Janeiro city, we explored the potential of IMERG products to monitor natural disaster triggers in the city. To derive urban flood and landslide triggering indicators from IMERG rainfall estimates, we used a state-of-the-art modeling system composed of the Noah-MP LSM, version 4.0.1, and high-resolution land surface parameters. We analyzed IMERG Early and IMERG Final rainfall estimates and rainfall-driven urban flood and landslide triggers (i.e., rootzone soil moisture and total runoff) and events that occurred during the wet season from 2001 to 2019 over urban and landslide-prone areas, using ground-based rainfall observations as reference. We found that long-term averaged IMERG products overestimate rainfall throughout the city and that impacts on TR and RZSM vary spatially as a function of land cover and soil types. We also noticed that IMERG-F generally outperforms IMERG-E, which could be explained by the additional adjustments with monthly gauge observations. However, due to its 2-month latency, IMERG-F was considered here as a benchmark for IMERG-E rather than a product that could be used for near real-time hazard warning systems. IMERG-based experiments resulted in a moderate performance to reproduce the spatial and temporal distribution of rainfall, TR and RZSM, and to quantitatively reproduce extreme events.

Based on our results and, more broadly, on previous studies using satellite precipitation data at a city scale, one can conclude that, IMERG’s 10-km spatial resolution is insufficient to capture local heterogeneities in cities with complex reliefs such as Rio de Janeiro. The inability to represent these complexities can have an enormous impact on the accuracy of landslide and urban flood early warning systems, since these occur at a very local scale. On the other hand, the temporal resolution and low latency (~4 h for IMERG Early) appear to be sufficient for rainfall-triggered disaster monitoring, particularly if the relative (e.g., percentile) distributions, rather than actual values, are considered. However, our results showed potential in qualitatively detecting city-wide extreme events after

normalizing signals through percentiles. POD values were above 0.5 for percentile thresholds as high as $\geq 90\%$, indicating that normalized IMERG-based experiments could be used to detect certain extreme events, supporting early warning systems and decision making related to natural disasters in the city.

This study evaluated the potential of IMERG to monitor natural disaster triggers in Rio de Janeiro. The next steps of this ongoing research will focus on evaluating its potential to support the operational monitoring and forecast actual natural disasters, in particular urban flood events across the city. It is also suggested that future work should focus on the improvement of algorithms and sensors to refine the detection of local heterogeneities, as well as reducing the latency of merged products.

Supplementary Materials: The following are available online at <http://www.mdpi.com/2072-4292/12/24/4095/s1>, Figure S1: POD and FAR maps for rainfall, RZSM and TR events derived from experiments with IMERG Early and IMERG Final at the percentile threshold $\geq 80\%$ chance of occurrence, Figure S2: POD and FAR maps for rainfall, RZSM and TR events derived from experiments with IMERG Early and IMERG Final at the percentile threshold $\geq 90\%$ chance of occurrence, Figure S3: POD and FAR maps for rainfall, RZSM and TR events derived from experiments with IMERG Early and IMERG Final at the percentile threshold $\geq 95\%$ chance of occurrence, Figure S4: POD and FAR maps for rainfall, RZSM and TR events derived from experiments with IMERG Early and IMERG Final at the percentile threshold $\geq 98\%$ chance of occurrence.

Author Contributions: Conceptualization, A.G.; methodology, A.G., D.K.; software, A.G., K.A.; validation, A.G., D.K., S.K.; formal analysis, A.G.; investigation, A.G.; resources, A.G., D.K.; data curation, A.G., F.M., M.O.; writing—original draft preparation, A.G.; writing—review and editing, A.G., D.K., F.M., M.O., S.K., K.A.; visualization, A.G.; supervision, A.G.; project administration, A.G., D.K., F.M.; funding acquisition, D.K. All authors have read and agreed to the published version of the manuscript.

Funding: This research was funded by NASA's Applied Sciences Program.

Acknowledgments: We would like to thank J.F. Lumberras (Embrapa Soils, Brazil) for the technical support in the Rio de Janeiro soil texture classification, and to Rio de Janeiro's Municipal Environment Secretariat and Pereira Passos Institute staffs for the technical support on land cover data processing. Computing resources supporting this work were provided by the NASA High-End Computing (HEC) Program through the NASA Center for Climate Simulation (NCCS) at NASA's Goddard Space Flight Center.

Conflicts of Interest: The authors declare no conflict of interest.

References

- Mitchell, J.K. Megacities and natural disasters: A comparative analysis. *GeoJournal* **1999**, *49*, 137–142. [[CrossRef](#)]
- Ogie, R.I.; Adam, C.; Perez, P. A review of structural approach to flood management in coastal megacities of developing nations: Current research and future directions. *J. Environ. Plan. Manag.* **2020**, *63*, 127–147. [[CrossRef](#)]
- ELLA. *Urban Disaster Risk Management in Latin American Cities; Evidence and Lessons from Latin America*: Lima, Peru, 2017; Volume 13.
- Miguez, M.G.; Veról, A.P.; Bianchini, L. Flood risk assessment and management: A case study in Rio de Janeiro. *WIT Trans. Built Environ.* **2013**, *134*, 29–41. [[CrossRef](#)]
- Diaz, V.J. Landslides in the squatter settlements of Caracas; towards a better understanding of causative factors. *Environ. Urban.* **1992**, *4*, 80–89. [[CrossRef](#)]
- Haigh, M.; Rawat, J.S. Landslide causes: Human impacts on a Himalayan landslide swarm. *Belgeo* **2011**, 201–220. [[CrossRef](#)]
- Cui, Y.; Cheng, D.; Choi, C.E.; Jin, W.; Lei, Y.; Kargel, J.S. The cost of rapid and haphazard urbanization: Lessons learned from the Freetown landslide disaster. *Landslides* **2019**, *16*, 1167–1176. [[CrossRef](#)]
- Lo, S.-W.; Wu, J.-H.; Lin, F.-P.; Hsu, C.-H. Visual Sensing for Urban Flood Monitoring. *Sensors* **2015**, *15*, 20006–20029. [[CrossRef](#)]
- Garcia, F.C.C.; Retamar, A.E.; Javier, J.C. A real time urban flood monitoring system for metro Manila. In Proceedings of the TENCON 2015—2015 IEEE Region 10 Conference, Macao, China, 1–4 November 2015; IEEE: Piscataway, NJ, USA, 2015; pp. 1–5.
- Hsu, S.-Y.; Chen, T.-B.; Du, W.-C.; Wu, J.-H.; Chen, S.-C. Integrate Weather Radar and Monitoring Devices for Urban Flooding Surveillance. *Sensors* **2019**, *19*, 825. [[CrossRef](#)]

11. Wang, R.-Q.; Mao, H.; Wang, Y.; Rae, C.; Shaw, W. Hyper-resolution monitoring of urban flooding with social media and crowdsourcing data. *Comput. Geosci.* **2018**, *111*, 139–147. [[CrossRef](#)]
12. Chen, Y.; Zhou, H.; Zhang, H.; Du, G.; Zhou, J. Urban flood risk warning under rapid urbanization. *Environ. Res.* **2015**, *139*, 3–10. [[CrossRef](#)]
13. Leitão, J.P.; Simões, N.E.; Maksimović, Č.; Ferreira, F.; Prodanović, D.; Matos, J.S.; Sá Marques, A. Real-time forecasting urban drainage models: Full or simplified networks? *Water Sci. Technol.* **2010**, *62*, 2106–2114. [[CrossRef](#)] [[PubMed](#)]
14. Ozdemir, H.; Sampson, C.C.; De Almeida, G.A.M.; Bates, P.D. Evaluating scale and roughness effects in urban flood modelling using terrestrial LIDAR data. *Hydrol. Earth Syst. Sci.* **2013**, *17*, 4015–4030. [[CrossRef](#)]
15. Sampson, C.C.; Bates, P.D.; Neal, J.C.; Horritt, M.S. An automated routing methodology to enable direct rainfall in high resolution shallow water models. *Hydrol. Process.* **2013**, *27*, 467–476. [[CrossRef](#)]
16. Newman, A.J.; Clark, M.P.; Sampson, K.; Wood, A.; Hay, L.E.; Bock, A.; Viger, R.J.; Blodgett, D.; Brekke, L.; Arnold, J.R.; et al. Development of a large-sample watershed-scale hydrometeorological data set for the contiguous USA: Data set characteristics and assessment of regional variability in hydrologic model performance. *Hydrol. Earth Syst. Sci.* **2015**, *19*, 209–223. [[CrossRef](#)]
17. Miguez, M.G.; Battemarco, B.P.; De Sousa, M.M.; Rezende, O.M.; Veról, A.P.; Gusmaroli, G. Urban Flood Simulation Using MODCEL—An Alternative Quasi-2D Conceptual Model. *Water* **2017**, *9*, 445. [[CrossRef](#)]
18. Varlas, G.; Anagnostou, M.N.; Spyrou, C.; Papadopoulos, A.; Kalogiros, J.; Mentzafou, A.; Michaelides, S.; Baltas, E.; Karymbalis, E.; Katsafados, P. A Multi-Platform Hydrometeorological Analysis of the Flash Flood Event of 15 November 2017 in Attica, Greece. *Remote Sens.* **2018**, *11*, 45. [[CrossRef](#)]
19. Schumann, G.J.-P.; Neal, J.C.; Mason, D.C.; Bates, P.D. The accuracy of sequential aerial photography and SAR data for observing urban flood dynamics, a case study of the UK summer 2007 floods. *Remote Sens. Environ.* **2011**, *115*, 2536–2546. [[CrossRef](#)]
20. Feng, Q.; Liu, J.; Gong, J. Urban Flood Mapping Based on Unmanned Aerial Vehicle Remote Sensing and Random Forest Classifier—A Case of Yuyao, China. *Water* **2015**, *7*, 1437–1455. [[CrossRef](#)]
21. Neal, J.; Schumann, G.; Fewtrell, T.; Budimir, M.; Bates, P.; Mason, D. Evaluating a new LISFLOOD-FP formulation with data from the summer 2007 floods in Tewkesbury, UK. *J. Flood Risk Manag.* **2011**, *4*, 88–95. [[CrossRef](#)]
22. Segoni, S.; Battistini, A.; Rossi, G.; Rosi, A.; Lagomarsino, D.; Catani, F.; Moretti, S.; Casagli, N. Technical Note: An operational landslide early warning system at regional scale based on space–time-variable rainfall thresholds. *Nat. Hazards Earth Syst. Sci.* **2015**, *15*, 853–861. [[CrossRef](#)]
23. Piciullo, L.; Dahl, M.-P.; Devoli, G.; Colleuille, H.; Calvello, M. Adapting the EDuMaP method to test the performance of the Norwegian early warning system for weather-induced landslides. *Nat. Hazards Earth Syst. Sci.* **2017**, *17*, 817–831. [[CrossRef](#)]
24. Rosi, A.; Canavesi, V.; Segoni, S.; Dias Nery, T.; Catani, F.; Casagli, N. Landslides in the Mountain Region of Rio de Janeiro: A Proposal for the Semi-Automated Definition of Multiple Rainfall Thresholds. *Geosciences* **2019**, *9*, 203. [[CrossRef](#)]
25. Segoni, S.; Piciullo, L.; Gariano, S.L. A review of the recent literature on rainfall thresholds for landslide occurrence. *Landslides* **2018**, *15*, 1483–1501. [[CrossRef](#)]
26. Guzzetti, F.; Gariano, S.L.; Peruccacci, S.; Brunetti, M.T.; Marchesini, I.; Rossi, M.; Melillo, M. Geographical landslide early warning systems. *Earth-Science Rev.* **2020**, *200*, 102973. [[CrossRef](#)]
27. Kirschbaum, D.; Stanley, T. Satellite-Based Assessment of Rainfall-Triggered Landslide Hazard for Situational Awareness. *Earth's Futur.* **2018**, *6*, 505–523. [[CrossRef](#)]
28. Huffman, G.J.; Bolvin, D.T.; Nelkin, E.J.; Wolff, D.B.; Adler, R.F.; Gu, G.; Hong, Y.; Bowman, K.P.; Stocker, E.F. The TRMM Multisatellite Precipitation Analysis (TMPA): Quasi-Global, Multiyear, Combined-Sensor Precipitation Estimates at Fine Scales. *J. Hydrometeorol.* **2007**, *8*, 38–55. [[CrossRef](#)]
29. Hou, A.Y.; Kakar, R.K.; Neeck, S.; Azarbarzin, A.A.; Kummerow, C.D.; Kojima, M.; Oki, R.; Nakamura, K.; Iguchi, T. The Global Precipitation Measurement Mission. *Bull. Am. Meteorol. Soc.* **2014**, *95*, 701–722. [[CrossRef](#)]
30. Skofronick-Jackson, G.; Petersen, W.A.; Berg, W.; Kidd, C.; Stocker, E.F.; Kirschbaum, D.B.; Kakar, R.; Braun, S.A.; Huffman, G.J.; Iguchi, T.; et al. The Global Precipitation Measurement (GPM) Mission for Science and Society. *Bull. Am. Meteorol. Soc.* **2017**, *98*, 1679–1695. [[CrossRef](#)]

31. Kirschbaum, D.B.; Huffman, G.J.; Adler, R.F.; Braun, S.; Garrett, K.; Jones, E.; McNally, A.; Skofronick-Jackson, G.; Stocker, E.; Wu, H.; et al. NASA's Remotely Sensed Precipitation: A Reservoir for Applications Users. *Bull. Am. Meteorol. Soc.* **2017**, *98*, 1169–1184. [[CrossRef](#)]
32. Khan, S.; Maggioni, V.; Kirstetter, P.-E. Investigating the Potential of Using Satellite-Based Precipitation Radars as Reference for Evaluating Multisatellite Merged Products. *J. Geophys. Res. Atmos.* **2018**, *123*, 8646–8660. [[CrossRef](#)]
33. Skofronick-Jackson, G.; Kirschbaum, D.; Petersen, W.; Huffman, G.; Kidd, C.; Stocker, E.; Kakar, R. The Global Precipitation Measurement (GPM) mission's scientific achievements and societal contributions: Reviewing four years of advanced rain and snow observations. *Q. J. R. Meteorol. Soc.* **2018**, *144*, 27–48. [[CrossRef](#)]
34. Kim, K.; Park, J.; Baik, J.; Choi, M. Evaluation of topographical and seasonal feature using GPM IMERG and TRMM 3B42 over Far-East Asia. *Atmos. Res.* **2017**, *187*, 95–105. [[CrossRef](#)]
35. Khodadoust Siuki, S.; Saghafian, B.; Moazami, S. Comprehensive evaluation of 3-hourly TRMM and half-hourly GPM-IMERG satellite precipitation products. *Int. J. Remote Sens.* **2017**, *38*, 558–571. [[CrossRef](#)]
36. Zubieta, R.; Getirana, A.; Espinoza, J.C.; Lavado-Casimiro, W.; Aragon, L. Hydrological modeling of the Peruvian-Ecuadorian Amazon Basin using GPM-IMERG satellite-based precipitation dataset. *Hydrol. Earth Syst. Sci.* **2017**, *21*, 3543–3555. [[CrossRef](#)] [[PubMed](#)]
37. Boone, A.; De Rosnay, P.; Balsamo, G.; Beljaars, A.; Chopin, F.; Decharme, B.; Delire, C.; Ducharne, A.; Gascoïn, S.; Grippa, M.; et al. The AMMA land surface model intercomparison project (ALMIP). *Bull. Am. Meteorol. Soc.* **2009**, *90*, 1865–1880. [[CrossRef](#)]
38. Getirana, A.; Espinoza, J.; Ronchail, J.; Rotunno Filho, O.C. Assessment of different precipitation datasets and their impacts on the water balance of the Negro River basin. *J. Hydrol.* **2011**, *404*, 304–322. [[CrossRef](#)]
39. Gebregiorgis, A.S.; Kirstetter, P.; Hong, Y.E.; Gourley, J.J.; Huffman, G.J.; Petersen, W.A.; Xue, X.; Schwaller, M.R. To What Extent is the Day 1 GPM IMERG Satellite Precipitation Estimate Improved as Compared to TRMM TMPA-RT? *J. Geophys. Res. Atmos.* **2018**, *123*, 1694–1707. [[CrossRef](#)]
40. Prakash, S.; Mitra, A.K.; AghaKouchak, A.; Liu, Z.; Norouzi, H.; Pai, D.S. A preliminary assessment of GPM-based multi-satellite precipitation estimates over a monsoon dominated region. *J. Hydrol.* **2018**, *556*, 865–876. [[CrossRef](#)]
41. Rozante, J.; Vila, D.; Barboza Chiquetto, J.; Fernandes, A.; Souza Alvim, D. Evaluation of TRMM/GPM Blended Daily Products over Brazil. *Remote Sens.* **2018**, *10*, 882. [[CrossRef](#)]
42. Huffman, G.; Bolvin, D.T.; Braithwaite, D.; Hsu, K.; Joyce, R.; Kidd, C.; Nelkin, E.J.; Xie, P. *NASA Global Precipitation Measurement (GPM) Integrated Multi-satellitE Retrievals for GPM (IMERG) Prepared for: Global Precipitation Measurement (GPM) National Aeronautics and Space Administration (NASA); Algorithm Theoretical Basis Document Version 4.5; National Aeronautics and Space Administration: Washington, DC, USA, 2015; 26p.*
43. Tan, M.; Duan, Z. Assessment of GPM and TRMM Precipitation Products over Singapore. *Remote Sens.* **2017**, *9*, 720. [[CrossRef](#)]
44. Floodlist Brazil—10 Dead After Torrential Rain in Rio de Janeiro. Available online: <http://floodlist.com/america/brazil-rio-floods-april-2019> (accessed on 29 June 2020).
45. Floodlist Brazil—Deadly Floods and Landslides in Rio de Janeiro After 90 mm of Rain in 1 Hour. Available online: <http://floodlist.com/america/brazil-rio-de-janeiro-flood-storm-february-2019> (accessed on 29 June 2020).
46. Fonseca, P.; Gaier, R.V. Powerful, “Abnormal” Rains Lash Rio de Janeiro, at Least Six Dead. Available online: <https://www.reuters.com/article/us-brazil-weather/powerful-abnormal-rains-lash-rio-de-janeiro-at-least-six-dead-idUSKCN1RL20U> (accessed on 29 June 2020).
47. Jeantet, D. Heavy Rains Cause Deadly Floods in Rio de Janeiro. Available online: <https://www.pbs.org/newshour/world/heavy-rains-cause-deadly-floods-in-rio-de-janeiro> (accessed on 29 June 2020).
48. Kumar, S.V.; Peters-Lidard, C.D.; Tian, Y.; Houser, P.R.; Geiger, J.; Olden, S.; Lighty, L.; Eastman, J.L.; Doty, B.; Dirmeyer, P.; et al. Land information system: An interoperable framework for high resolution land surface modeling. *Environ. Model. Softw.* **2006**, *21*, 1402–1415. [[CrossRef](#)]
49. Arsenault, K.R.; Kumar, S.V.; Geiger, J.V.; Wang, S.; Kemp, E.; Mocko, D.M.; Beaudoin, H.K.; Getirana, A.; Navari, M.; Li, B.; et al. The Land surface Data Toolkit (LDT v7.2)—A data fusion environment for land data assimilation systems. *Geosci. Model Dev.* **2018**, *11*, 3605–3621. [[CrossRef](#)]

50. Yang, Z.-L.; Niu, G.-Y.; Mitchell, K.E.; Chen, F.; Ek, M.B.; Barlage, M.; Longuevergne, L.; Manning, K.; Niyogi, D.; Tewari, M.; et al. The community Noah land surface model with multiparameterization options (Noah-MP): 2. Evaluation over global river basins. *J. Geophys. Res. Atmos.* **2011**, *116*. [[CrossRef](#)]
51. Niu, G.-Y.; Yang, Z.-L.; Mitchell, K.E.; Chen, F.; Ek, M.B.; Barlage, M.; Kumar, A.; Manning, K.; Niyogi, D.; Rosero, E.; et al. The community Noah land surface model with multiparameterization options (Noah-MP): 1. Model description and evaluation with local-scale measurements. *J. Geophys. Res. Atmos.* **2011**, *116*, 1–19. [[CrossRef](#)]
52. Ek, M.B.; Mitchell, K.E.; Lin, Y.; Rogers, E.; Grunmann, P.; Koren, V.; Gayno, G.; Tarpley, J.D. Implementation of Noah land surface model advances in the National Centers for Environmental Prediction operational mesoscale Eta model. *J. Geophys. Res. Atmos.* **2003**, *108*. [[CrossRef](#)]
53. Ball, J.T.; Woodrow, I.E.; Berry, J.A. A Model Predicting Stomatal Conductance and its Contribution to the Control of Photosynthesis under Different Environmental Conditions. In *Progress in Photosynthesis Research*; Springer: Dordrecht, The Netherlands, 1987; pp. 221–224.
54. Niu, G.-Y.; Yang, Z.-L.; Dickinson, R.E.; Gulden, L.E.; Su, H. Development of a simple groundwater model for use in climate models and evaluation with Gravity Recovery and Climate Experiment data. *J. Geophys. Res.* **2007**, *112*, D07103. [[CrossRef](#)]
55. Campbell, P.C.; Bash, J.O.; Spero, T.L. Updates to the Noah Land Surface Model in WRF-CMAQ to Improve Simulated Meteorology, Air Quality, and Deposition. *J. Adv. Model. Earth Syst.* **2019**, *11*, 231–256. [[CrossRef](#)]
56. Schueler, T.R. The Compaction of Urban Soils. In *The Practice of Watershed Protection*; Schueler, T.R., Holland, H.K., Eds.; Center for Watershed Protection: Ellicott City, MD, USA, 2000; pp. 661–665.
57. Csizar, I.; Gutman, G. Mapping global land surface albedo from NOAA AVHRR. *J. Geophys. Res. Atmos.* **1999**, *104*, 6215–6228. [[CrossRef](#)]
58. Chen, F.; Mitchell, K.; Schaake, J.; Xue, Y.; Pan, H.-L.; Koren, V.; Duan, Q.Y.; Ek, M.; Betts, A. Modeling of land surface evaporation by four schemes and comparison with FIFE observations. *J. Geophys. Res. Atmos.* **1996**, *101*, 7251–7268. [[CrossRef](#)]
59. Monin, A.S.; Obukhov, A.M. Basic laws of turbulent mixing in the surface layer of the atmosphere. *Tr. Akad. Nauk. SSSR Geophys. Inst.* **1954**, *24*, 163–187.
60. Niu, G.-Y.; Yang, Z.-L. Effects of Frozen Soil on Snowmelt Runoff and Soil Water Storage at a Continental Scale. *J. Hydrometeorol.* **2006**, *7*, 937–952. [[CrossRef](#)]
61. Niu, G.-Y.; Yang, Z.-L. Effects of vegetation canopy processes on snow surface energy and mass balances. *J. Geophys. Res. Atmos.* **2004**, *109*. [[CrossRef](#)]
62. Cosgrove, B.A.; Lohmann, D.; Mitchell, K.E.; Houser, P.R.; Wood, E.F.; Schaake, J.C.; Robock, A.; Marshall, C.; Sheffield, J.; Duan, Q.; et al. Real-time and retrospective forcing in the North American Land Data Assimilation System (NLDAS) project. *J. Geophys. Res. Atmos.* **2003**, *108*, 2002JD003118. [[CrossRef](#)]
63. Shepard, D. A two-dimensional interpolation function for irregularly-spaced data. In Proceedings of the 1968 23rd ACM national conference, Las Vegas, NV, USA, 27–29 August 1968; ACM Press: New York, NY, USA, 1968; pp. 517–524.
64. Salvatici, T.; Tofani, V.; Rossi, G.; D’Ambrosio, M.; Tacconi Stefanelli, C.; Masi, E.B.; Rosi, A.; Pazzi, V.; Vannocci, P.; Petrolo, M.; et al. Application of a physically based model to forecast shallow landslides at a regional scale. *Nat. Hazards Earth Syst. Sci.* **2018**, *18*, 1919–1935. [[CrossRef](#)]
65. Wickland, D.E. Mission to Planet Earth: The Ecological Perspective. *Ecology* **1991**, *72*, 1923–1933. [[CrossRef](#)]
66. Gomes, J.B.V.; Lumberras, J.F.; Palmieri, F.; Zaroni, M.J.; Oliveira, R.P.; Bhering, S.B.; Calderano, S.B.; Santos, H.G.; Cunha, T.J.F.; Aglio, M.L.D. Atualização do Levantamento Semidetalhado de Solos do Município do Rio de Janeiro, RJ. In *Mapeamento Pedológico e Interpretações Úteis ao Planejamento Ambiental do Município do Rio de Janeiro*; Lumberras, J.F., Gomes, J.B.V., Eds.; Embrapa Solos: Rio de Janeiro, Brazil, 2004; pp. 7–270, ISBN 85-85864-16-8.
67. Soil Survey Staff. *Keys to Soil Taxonomy*; Department of Agriculture, Natural Resources Conservation Service: Washington, DC, USA, 2014; Volume 12.
68. *Soil Science Division Staff Soil Survey Manual*; USDA Handbook 18; USDA: Washington, DC, USA, 2017; pp. 145–148. [[CrossRef](#)]
69. Embrapa. *Mapeamento Pedológico e Interpretações Úteis ao Planejamento Ambiental do Município do Rio de Janeiro*; Embrapa: Brasilia, Brazil, 2004; ISBN 8585864168.

70. GEORIO Rio de Janeiro City Landslide Susceptibility Map. Available online: <https://www.data.rio/app/suscetibilidade-a-deslizamentos> (accessed on 17 November 2020).
71. Xu, R.; Tian, F.; Yang, L.; Hu, H.; Lu, H.; Hou, A. Ground validation of GPM IMERG and TRMM 3B42V7 rainfall products over southern Tibetan Plateau based on a high-density rain gauge network. *J. Geophys. Res. Atmos.* **2017**, *122*, 910–924. [[CrossRef](#)]
72. Jiang, Q.; Li, W.; Wen, J.; Qiu, C.; Sun, W.; Fang, Q.; Xu, M.; Tan, J. Accuracy Evaluation of Two High-Resolution Satellite-Based Rainfall Products: TRMM 3B42V7 and CMORPH in Shanghai. *Water* **2018**, *10*, 40. [[CrossRef](#)]
73. Arsenault, K.R.; Shukla, S.; Hazra, A.; Getirana, A.; McNally, A.; Kumar, S.V.; Koster, R.D.; Peters-Lidard, C.D.; Zaitchik, B.F.; Badr, H.; et al. The NASA hydrological forecast system for food and water security applications. *Bull. Am. Meteorol. Soc.* **2020**. [[CrossRef](#)]
74. Getirana, A.; Rodell, M.; Kumar, S.; Beaudoin, H.K.; Arsenault, K.; Zaitchik, B.; Save, H.; Bettadpur, S. GRACE Improves Seasonal Groundwater Forecast Initialization over the United States. *J. Hydrometeorol.* **2020**, *21*, 59–71. [[CrossRef](#)]
75. Li, B.; Rodell, M.; Kumar, S.; Beaudoin, H.K.; Getirana, A.; Zaitchik, B.F.; Goncalves, L.G.; Cossetin, C.; Bhanja, S.; Mukherjee, A.; et al. Global GRACE Data Assimilation for Groundwater and Drought Monitoring: Advances and Challenges. *Water Resour. Res.* **2019**, 1–23. [[CrossRef](#)]
76. Svoboda, M.; LeComte, D.; Hayes, M.; Heim, R.; Gleason, K.; Angel, J.; Rippey, B.; Tinker, R.; Palecki, M.; Stooksbury, D.; et al. THE DROUGHT MONITOR. *Bull. Am. Meteorol. Soc.* **2002**, *83*, 1181–1190. [[CrossRef](#)]
77. Rozante, J.R.; Moreira, D.S.; de Goncalves, L.G.G.; Vila, D.A. Combining TRMM and Surface Observations of Precipitation: Technique and Validation over South America. *Weather Forecast.* **2010**, *25*, 885–894. [[CrossRef](#)]
78. Salamanca, F.; Zhang, Y.; Barlage, M.; Chen, F.; Mahalov, A.; Miao, S. Evaluation of the WRF-Urban Modeling System Coupled to Noah and Noah-MP Land Surface Models Over a Semiarid Urban Environment. *J. Geophys. Res. Atmos.* **2018**, *123*, 2387–2408. [[CrossRef](#)]
79. Paiva, R.C.D.; Buarque, D.C.; Collischonn, W.; Bonnet, M.P.; Frappart, F.; Calmant, S.; Bulhões Mendes, C.A. Large-scale hydrologic and hydrodynamic modeling of the Amazon River basin. *Water Resour. Res.* **2013**, *49*, 1226–1243. [[CrossRef](#)]
80. Harris, A.; Rahman, S.; Hossain, F.; Yarborough, L.; Bagtzoglou, A.; Eason, G. Satellite-based Flood Modeling Using TRMM-based Rainfall Products. *Sensors* **2007**, *7*, 3416–3427. [[CrossRef](#)]
81. Wright, D.B. Rainfall Information for Global Flood Modeling. In *Global Flood Hazard: Applications in Modeling, Mapping, and Forecasting*; Schumann, G.J., Bates, P.D., Apel, H., Aronica, G.T., Eds.; American Geophysical Union: Washington, DC, USA, 2018; pp. 17–42.

Publisher’s Note: MDPI stays neutral with regard to jurisdictional claims in published maps and institutional affiliations.



© 2020 by the authors. Licensee MDPI, Basel, Switzerland. This article is an open access article distributed under the terms and conditions of the Creative Commons Attribution (CC BY) license (<http://creativecommons.org/licenses/by/4.0/>).